Fine-Scale Heterogeneity of Pyrite and Organics within Mudrocks: Scanning Electron Microscopy and Image Analysis at the Large Scale

Jim Buckman, Anabel Aboussou, Onoriode Esegbue, Thomas O Wagner, Gabriele Gambacorta

minerals

MDPI

Article

Fine-Scale Heterogeneity of Pyrite and Organics within Mudrocks: Scanning Electron Microscopy and Image Analysis at the Large Scale

Jim Buckman [1,*], Anabel Aboussou [2], Onoriode Esegbue [3], Thomas Wagner [3] and Gabriele Gambacorta [4]

1 Institute of GeoEnergy Engineering, School of Energy, Geoscience, Infrastructure and Society, Heriot-Watt University, Riccarton, Edinburgh EH14 4AS, UK
2 IFP Energies Nouvelles, 1-4 Avenue du bois Préau 92852 Rueil-Malmaison, 92852 Paris, France; anabelaboussou@yahoo.fr
3 Lyell Centre, Heriot-Watt University, Riccarton, Edinburgh EH14 4AS, UK; o.esegbue@hw.ac.uk (O.E.); t.wagner@hw.ac.uk (T.W.)
4 Eni S.p.A., Upstream and Technical Services, Geology and Geophysics Research and Technological Innovation Department, Via Emilia 1, 20097 San Donato Milanese, Italy; gabriele.gambacorta@eni.com
* Correspondence: j.buckman@hw.ac.uk

Received: 26 March 2020; Accepted: 13 April 2020; Published: 16 April 2020

Abstract: Mudrocks are highly heterogeneous in terms of both composition and fabric, with heterogeneities occurring at the submicron to centimetre plus scale. Such heterogeneities are relatively easy to visualise at the micron-scale through the use of modern scanning electron microscopy (SEM) techniques, but due to their inherent fine grain size, can be difficult to place within the greater context of the mudrock as a whole, or to visualise variation when viewed at a centimetre scale. The utilisation of SEM to collect automated high-resolution backscattered (BSE) images (tiles) over whole, polished thin-sections presents a potential large data bank on compositional and fabric changes that can be further processed using simple image analysis techniques to extract data on compositional variation. This can then be plotted graphically in 2D as colour contoured distribution maps to illustrate any observed variability. This method enables the easy visualisation of micron-scale heterogeneity present in mudrock, which are here illustrated and discussed for pyrite and organic content at the larger (thin-section) centimetre scale. This does not require the use of other techniques such as energy dispersive x-ray (EDX) mapping to identify phases present, but instead utilizes BSE images that may already have been collected for textural fabric studies. The technique can also be applied to other phases in mudrocks, such as carbonates and silicates, as well as porosity. Data can also be extracted and used in a similar fashion to bulk compositional analytical techniques such as inductively coupled plasma-atomic emission microscopy (ICP-AES) and carbon, nitrogen and sulphur (CNS) analysis, for average organic carbon and percentage pyrite.

Keywords: mudstones; high-resolution; large area format; porosity; organics; SEM

1. Introduction

Mudrocks are one of the most ubiquitous sedimentary materials, both on the Earth's surface and in terms of stratigraphic distribution [1–4], and are of great significance as seals/traps for oil and gas reservoirs, for the confinement of aquifers, for CO_2 seals, for nuclear and urban waste, for conventional and unconventional source rocks and for reservoirs, in the formation of structural foundations, and important repositories of past environmental records [5–11]. Although at the macro level mudrocks are visually monotonous, on closer inspection, they are a highly heterogeneous sedimentary

rock group, varying widely in terms of colour, sedimentary structures, fissility, grain-size (clay and silt-sized), grain orientation, mineralogy, organic content, microfauna-macrofauna, ichofauna-fabric, porosity, permeability and diagenetic history [12–16]. Heterogeneity can be recognised at the micron, millimetre, centimetre and metre scales.

The fine-grained nature of mudrocks (clays 1–3 microns and silt particles up to 62 microns) limits the usefulness of optical microscopy and simple macro-visual techniques, although it is suitable for some characteristics, such as colour, fissility, sedimentary structures, macrofauna and ichnofabric. However, emphasis on detailed analysis typically requires the use of scanning electron microscopy (SEM) or, in some cases, transmission electron microscopy (TEM). The high-resolution nature of the studies required to characterise many of the heterogeneities within mudrocks causes a potential conundrum, in as much that although high-resolution imaging/analysis is possible, because of high costs and time constraints, it is not always possible to image large areas (at high-resolution) to allow lateral and vertical changes to be observed. Additionally, even where large-scale areas are imaged at high-resolution utilizing automated imaging protocols [17,18], it is typically not possible to observe small-scale heterogeneity within its context when viewed at the centimetre scale/whole thin-section level [19].

The current work utilizes a technique that has been successfully developed to visualise porosity within carbonates [20,21], and expands upon its use within mudrocks briefly outlined elsewhere [19]. The workflow for mudrock polished thin-sections provides a simple means of visualising heterogeneity in mineralogy (pyrite, organics, carbonates, silicates, etc.) and porosity through coloured contour distribution maps. Knowledge of the heterogeneity of such components within mudrock can be of great importance in environmental interpretation, hydrocarbon generation and production, and for the effectiveness of mudstones as seals for hydrocarbons and radioactive waste materials. Here we use the technique to examine two groups of mudrock samples, one looking at pyrite distribution, and the other at organic material distribution. A by-product of producing the contoured distribution maps is the ability to additionally extract information on bulk composition values through the averaging of data extracted during the image analysis process. In addition, we discuss other potential areas of use for the technique in connection to mudrocks.

2. Materials and Methods

Two groups of samples were examined:

1. Thirteen Jurassic (Toarcian) mudstones from the Grey Shale Member, at the base of the Whitby Mudstone Formation, Cleveland Basin, NE England [22], with a variety of pyrite distributions, approximately 1–16%.
2. Six Cretaceous ultra-deep-water mudstones (Southern Atlantic Margin), with a range of total organic carbon (TOC) content of approximately 2%, 4%, 15%, 26%, 36% and 48%. Two samples from Deep Sea Drilling Program (DSDP) site 364 (Kwanza Basin), continental slope (11°34.32′ S, 11°58.30′ E), water depth 2448 m, samples approximately 1000 m below sea floor. Two samples from Ocean Drilling Program (ODP) 959 Hole D (Tano Basin), on the continental slope margin (3°37.656′ N, 2°44.149′ W), water depth 2102 m, samples approximately 1000 m below sea floor. One sample from ODP 962 Hole D (Tano Basin), on the marginal ridge (3°15.082′ N, 3°10.898′ W), water depth 4650 m, 157 m below sea floor. One sample from DSDP 367 (Mauritania-Senegal-Guinea Bissau Basin), from the Abyssal Plain (120°29.2′ N, 200°02.8′ W), water depth 4748 m, 641 m below sea floor.

2.1. Scanning Electron Microscopy

The current work utilised a Quanta 650 FEG scanning electron microscope (SEM, Thermo Fisher Scientific, Waltham, MA, USA), which was used for its stability, allowing for the automated collection of a series of consecutive images (tiles) over time (up to 36 h) with minimal degradation or change in image quality in terms of brightness and contrast. The collection of high-resolution individual tiles

(100 to 200 µm horizontal field of view) from areas up to several square centimetres in size [18,20] was accomplished using 'MAPS' software (FEI, Hillsboro, OR, USA) from polished thin-sections.

2.2. Image Analysis and Processing

Individual collected images (tiles) were batch processed using 'Fiji' (open source software, Wayne Rasband, National Institutes of Health, Bethesda, MD, USA) where they were thresholded for either pyrite or organic material, binarized and had percentage coverage determined. Values obtained through 'Fiji' were used to calculate average percentage values, and the values for individual tiles were then plotted using 'MATLAB' (MathWorks Inc, Natick, MA, USA) on a grid framework corresponding to the dimensions of the area imaged, with values represented as a coloured contour map [18]. The full workflow has been previously illustrated in Buckman et al. [18]. In both cases, values obtained using the current method were compared with independently derived values.

2.3. Pyrite Elemental Analysis Method

Pyrite percentage for each sample had previously been independently obtained as part of a pyritic and organic sulphur quantification in which hydrofluoric and hydrochloric acids were used to isolate kerogen, pyrite and other minor oxides from the samples [22]. The total iron content was then quantified by inductively coupled plasma atomic emission spectroscopy (ICP-AES), and the total sulphur by Infrared spectroscopy (both at Standard Global Service France). The pyrite content was then stoichiometrically calculated, with the assumption that all iron is exclusively from pyrite (FeS_2), which is an oversimplification [23] and, therefore, may introduce significant errors, although it appears to be a reasonable assumption from SEM analysis.

2.4. Total Organic Carbon (TOC) Content Method

Samples had previously been analysed for total organic carbon (TOC) content based upon the technique from Krom and Berner [24]. Analyses was carried out at the Lyell Centre (Heriot-Watt University) with an aliquot (approximately 100 mg) of the pulverised core samples weighed and placed inside a porous crucible. A reference sample of known TOC (JET-1) was equally weighed and replicated after every 20 samples to check for reproducibility of the results. Approximately 1 mL of 4 mol/L hydrochloric acid was added to the pulverised rock samples in the porous crucibles to remove inorganic carbonate ($CaCO_3$) leaving only the residual organic carbon in the sample. The acid was then allowed to drain from the samples in a fume cupboard for about 8 h, after which the samples were washed with DI water as needed. Thereafter, the crucibles were placed in the oven at 60 °C and left for 24 h to dry. Prior to sample analysis, the LECO TruMac CNS analyser instrument was calibrated using LECO standards (BBOT; ORE LRM; EDTA and Sulfamethazine) of known but variable carbon content. Comcat (approximately 1 g) was added to each sample to help facilitate combustion at 1350 °C. The results were reported as sample weight percent organic carbon.

3. Results and Discussion

3.1. Pyrite

The thirteen scanned Jurassic mudstone plots display a variety of pyrite distribution patterns, which can be subdivided into three distinctive forms, namely stratified (Figure 1), sparse pyrite (Figure 2) and complex (Figure 3). Stratified pyrite displays bedding parallel zones, with distinct pyrite percentage ranges within each zone. Zones are typically cyclic, alternating between low and higher concentrations of pyrite. In some cases, the variation in the presence of pyrite present can be subtle (Figure 1A), with percentage pyrite mainly constrained to 5% or less, with zones of 0–2% and 2–5%, and with localised "mottled" maxima of around 8%. In others, the concentration of pyrite is higher, with alternating zones of 0–4% and 5–11%, respectively (Figure 1B), or having a generally low background concentration of pyrite (less than 5%) but with sporadically occurring zones in which

pyrite concentration can vary from 10% to 30–40% (Figure 1D,E). Some of the thin sections used (Figure 1A–C,F) contain bedding parallel cracks. With the region of interest currently used for each tile during the present study (200 µm HFOV), the finer cracks do not appear to impact on the final produced distribution maps (Figure 1A), although, as would be expected, thicker cracks are recorded on maps as layers of low pyrite concentration (Figure 1B). Although pyrite minima are not solely directly related to cracks, zones of lower concentration are typically found to be associated with such cracks (Figure 1B white arrows). This might suggest a weathering or diagenetic overprint, changing the pyrite concentration due to the presence of cracks.

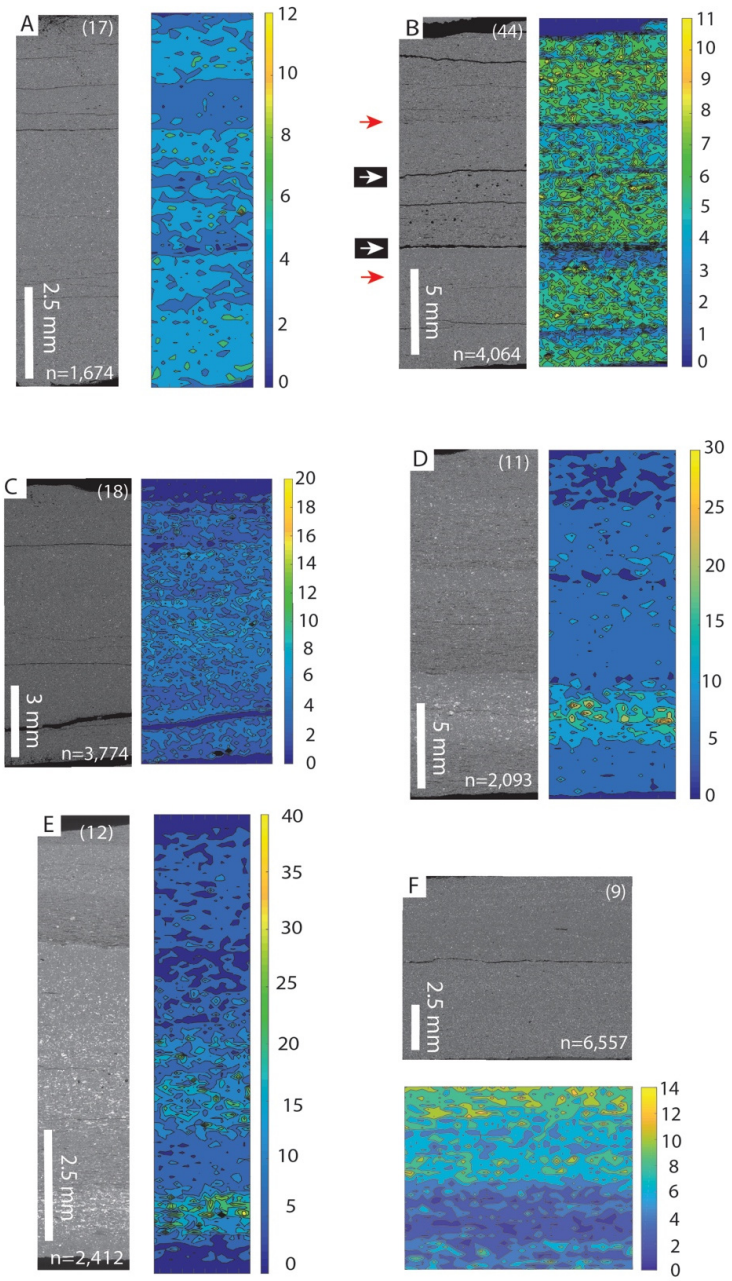

Figure 1. (**A**–**F**) Pairs of scanning electron microscopy backscattered electron montages and colour contoured pyrite distribution maps for six Jurassic mudstones illustrating stratified pyrite distribution. Figure at top right is sample number, and bottom right is the number of tiles in the montage. Individual tile horizontal field of view (HFOV) 200 µm. White arrows mark the position of sharp changes in pyrite% associated with cracks. Red arrows mark change not associated with cracks.

However, there is typically an asymmetric relationship of pyrite to cracks, with higher and lower laminae/bands of pyrite either side. Additionally, in some cases, the boundary between high and lower concentration zones is not marked by cracking (Figure 1B red arrows). It is, therefore, more likely that the cracks (partings) occur at junctions of pyrite concentration change (areas of weakness), occurring during unloading of the mudrock. Other mapped distributions of pyrite show a much lower occurrence (Figure 2). In these cases, although the background concentration is typically well under 5%, higher concentrations of pyrite (10–15%) can occasionally be observed as minor laminae (Figure 2A,B), spherical or ovoid clusters with concentrations from 20–60% (Figure 2C), or as sporadic minor fluctuations (less than 20%) in concentration (Figure 2D). Finally, some maps (Figure 3) display more complex patterns of pyrite concentration that do not conform to the stratified or other forms of noted distribution. In these samples, areas of low pyrite concentration appear to be associated with burrows (Figure 3A), lenticular or wavy bedforms (Figure 3B) or, in some cases, appear to be more irregular in nature (Figure 3C), with the latter in part possibly affected by artifacts such as holes introduced during sample preparation (Figure 3C, white arrows). For these more complex forms of pyrite distribution, it may be necessary to scan and construct larger area maps to better visualize pyrite distribution within the context of the larger sedimentological picture.

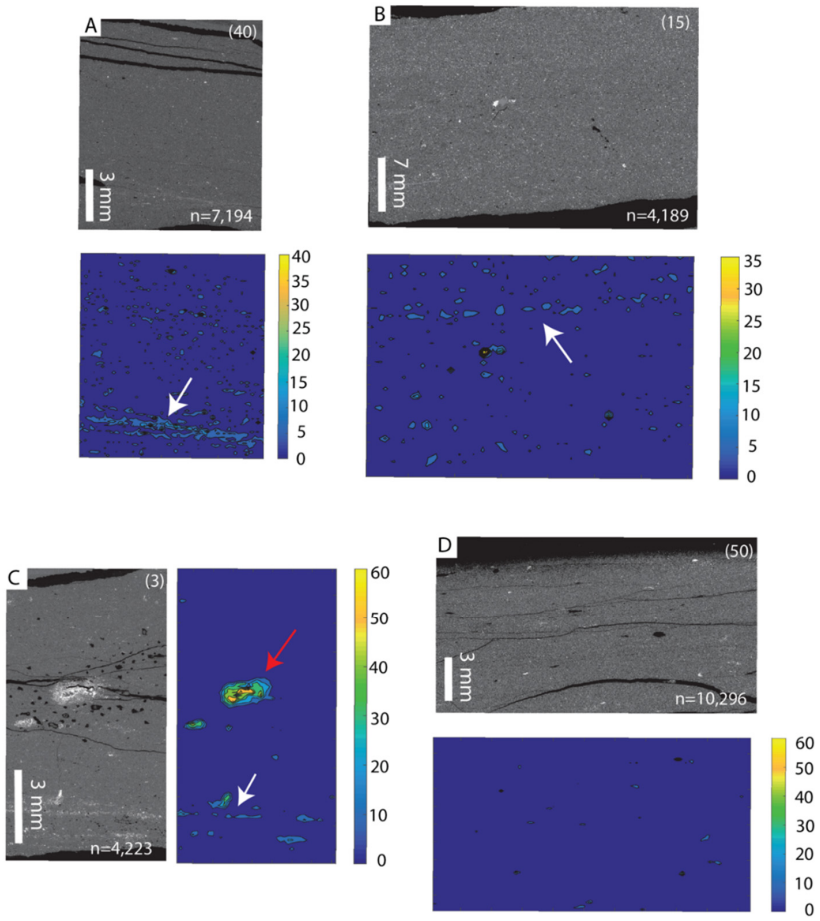

Figure 2. (**A**–**D**) Pairs of scanning electron microscopy backscattered electron montages and colour contoured pyrite distribution maps for four Jurassic mudstones illustrating sparse pyrite distribution. Figure at top right is sample number, and bottom right is the number of tiles in the montage. Each tile 200 µm horizontal field of view (HFOV). White arrows indicate minor pyrite laminae, and red arrow is a localised concentration.

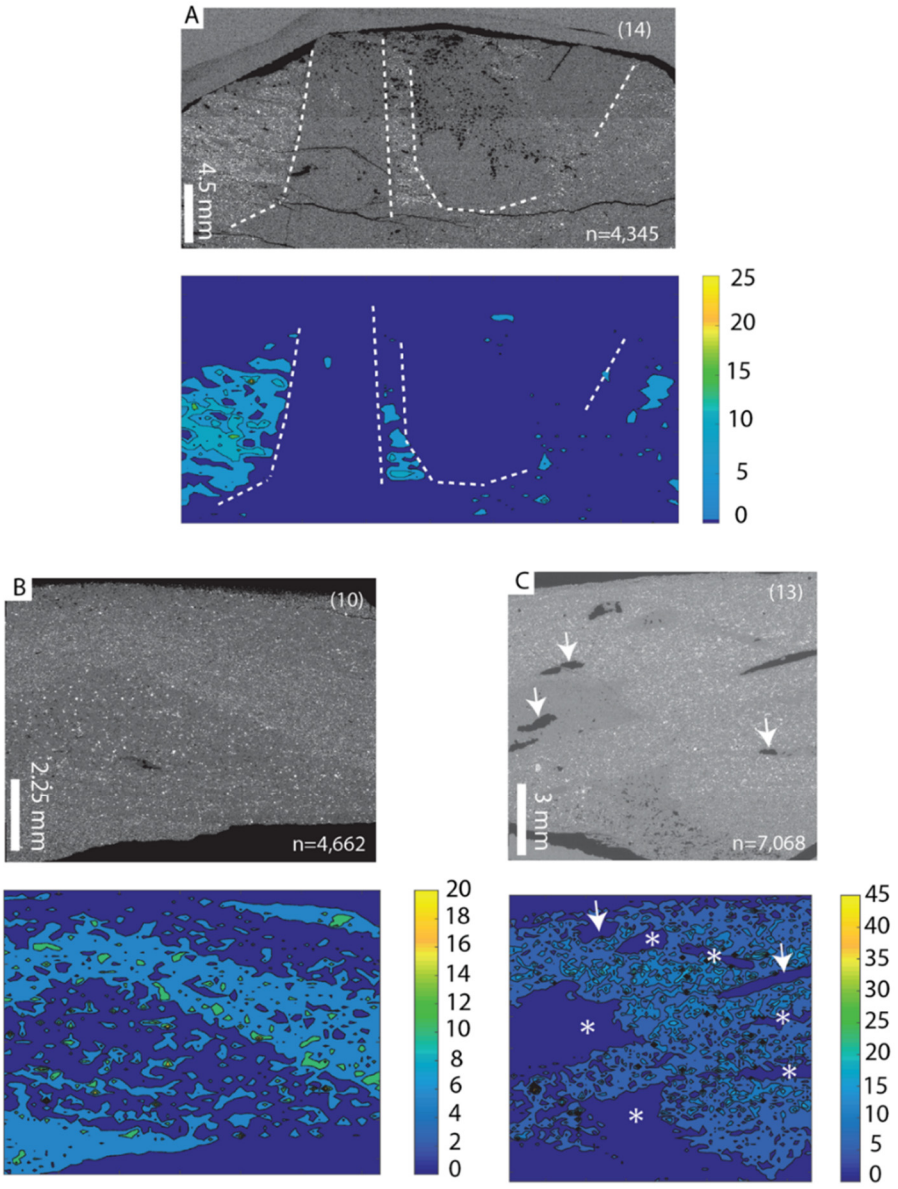

Figure 3. (**A**–**C**) Pairs of scanning electron microscopy backscattered electron montages and colour contoured pyrite distribution maps for three Jurassic mudstones illustrating complex pyrite distribution. Figure at top right is sample number, and bottom right is the number of tiles in the montage. Individual tile horizontal field of view (HFOV) 200 µm. Dashed line demarcates the boundary between higher and lower pyrite areas in association with burrows? White arrows relate to holes in the sample surface that are caused during preparation. White asterisk marks areas of genuine lower pyrite concentration.

The exact value recorded for percentage pyrite within each tile analysed will vary depending upon the size of the selected area of interest. Nevertheless, the current work allows the relative variation between parts of the mudstones to be shown, and all pyrite maps (Figures 1–3) clearly display microscale heterogeneities (vertical and lateral) within these mudstones. Due to the size of the selected area scanned, values recorded for percentage pyrite composition will therefore not necessarily conform to whole rock values. In this respect, plots of the average value for pyrite composition against whole rock pyrite values derived from ICP-AES measurements (Figure 4) are of interest. For those samples with sparse pyrite, three of the four samples are in close agreement. For the stratified samples (Figure 1), the majority of samples show lower figures for overall pyrite percentage compared to those achieved by ICP-AES, as do the 3 samples defined as having complex

pyrite distribution. The stratified sample (#17) that correlates well with both methods exhibits minimal variation between laminae, as well as an overall low pyrite concentration, similar to the low occurrence of pyrite from samples #3, #15 and #40. The discrepancies recorded for most of the stratified samples, and all of the complex samples, are not surprising, chiefly reflecting vertical and lateral heterogeneities, respectively. Given these heterogeneities, values recorded between the two methods (SEM vs ICP-AES) will potentially vary widely depending upon how closely the ICP-AES and SEM samples correlate in terms of area sampled. Samples with much lower values of pyrite are not strongly affected by the smaller localised heterogeneities.

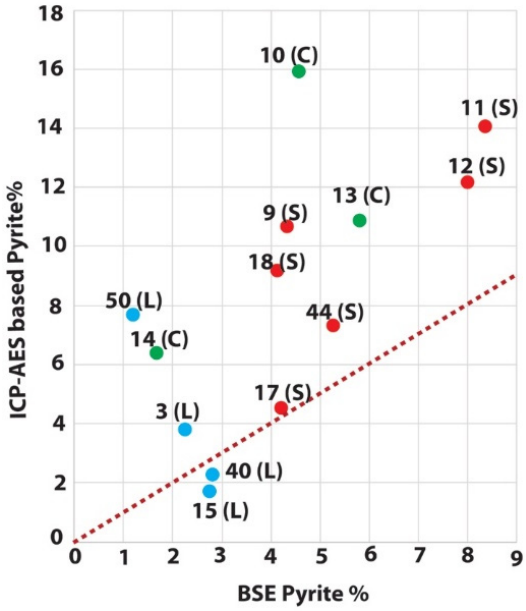

Figure 4. Graph illustrating the relationship between inductively coupled plasma-atomic emission spectroscopy (ICP-AES) based pyrite% and scanning electron microscopy (SEM) backscattered electron (BSE) based pyrite%. Red line is plotted along the axis representing an exact match.

3.2. Organics

Typical Backscattered images for each of the six selected samples show a progressive increase in organic (dark material) from sample to sample, which is in agreement with independently measured values for Total Organic Carbon (TOC) content (Figure 5). Contoured coloured maps for the two lowest TOC samples are reasonably 'homogenous' in form, while the higher TOC samples are variably laminated (clays, silicates, carbonates with organics), with increasing levels of discrete organic laminae (Figure 6). Contoured map plots generated for organic concentration show an increase in value (%), with a notable difference between low- and high-TOC samples. The sample with the lowest TOC value shows a general decrease in value from bottom to top (Figure 6A), while the next lowest is more homogeneously low, with occasional 'hot-spots' (Figure 6B). Maps for all of the laminated organic materials show much higher organic carbon content, which appear to be bedding parallel horizontally stratified, although due to the size of each scanned tile (200 µm HFOV), these do not reflect the exact position and number of laminae observed in the BSE montages, which are typically more in the order of 1 to 10 µm thick.

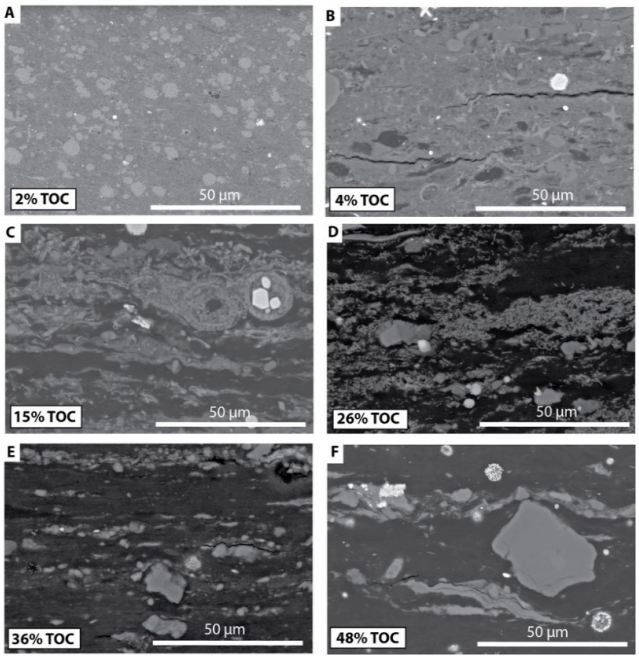

Figure 5. Single representative BSE tile images of the six organic samples examined. (**A**–**F**) 962D-6, 959D-48, 959D-58, 364-182, 367-20 and 364-205, respectively. Bottom left = recorded TOC from LECO CNS measurements. Note progressive increase in organic content (dark) in BSE images.

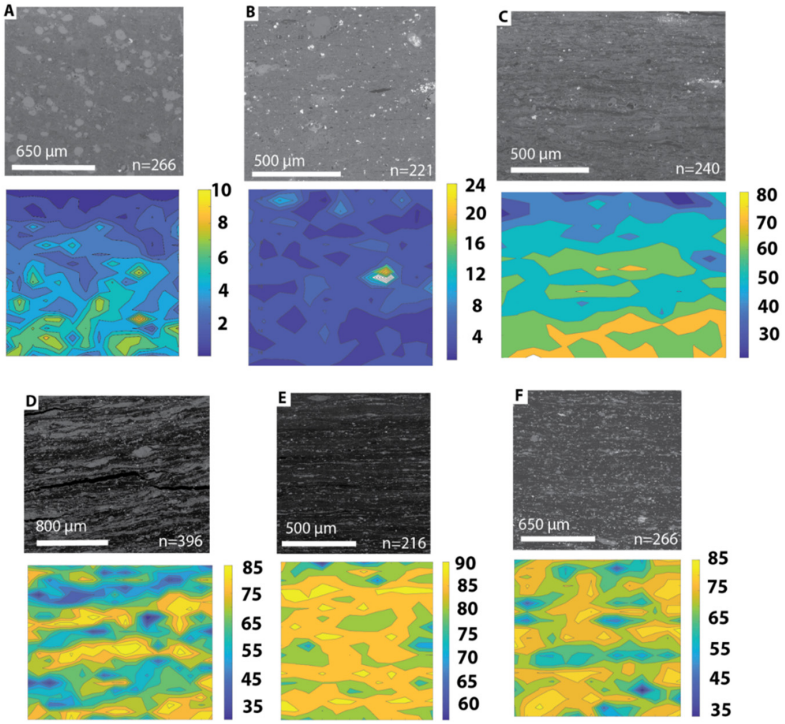

Figure 6. (**A**–**F**) Pairs of scanning electron microscopy backscattered electron montages and colour contoured organics distribution maps for six Cretaceous mudstones illustrating the distribution of organics. Figure at bottom right = number of tiles in the montage; each tile has a 100 µm horizontal field of view (HFOV). Samples arranged in the same order as Figure 5.

Values calculated for the percentage of organic carbon from tiles and montages (Figure 7) are close to the recorded TOC values for the two low-TOC samples, whereas for the higher TOC samples, averages for the organic carbon from individual tiles are two to four times higher than recorded TOC,

and for the montages it is in the region of two times higher. One exception is the highest TOC sample, where the calculated percentage for organic carbon from the montage closely matches that of the measured TOC.

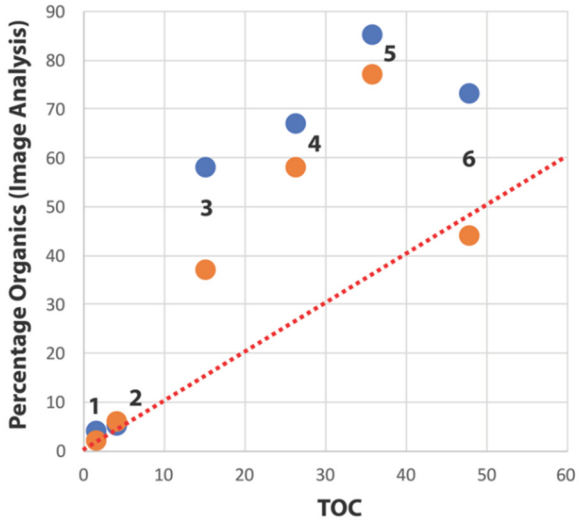

Figure 7. Graph illustrating the relationship between TOC and SEM BSE based organic%. Orange = TOC calculated from whole montage versus TOC from whole rock analysis; blue = average TOC calculated from individual tiles versus TOC from whole rock analysis. Red line is plotted along the axis representing an exact match. In general, a better match is seen between organic content calculated from montages versus whole rock analysis TOC. Key: 1 = 962D-6, 2 = 959D-48, 3 = 959D-58, 4 = 364-182, 5 = 367-20 and 6 = 364-205, respectively.

All examples illustrated in Figure 6 are for areas of around 1 mm^2. Nevertheless, the technique has good potential as both a visual indicator of organic content heterogeneity and total organic content. Two larger area sets of tiles (2850 and 1848 sets of 60 µm HFOV tiles) were collected for sample #959D-48 (Figure 8). These clearly illustrate the potential for imaging lateral and vertical heterogeneity within mudstones. This relatively low-TOC sample is fairly homogeneous, with most under 6%, but with some areas up to 20%. The apparent bright-spot near the centre of Figure 8C is due to the presence of debris on the surface of the slide.

The large discrepancy in the calculated organic percentage for the sample with the highest recorded TOC level (#364-205) is of particular interest. This may reflect differences in thresholding between the individual tiles and full montage (which were independently thresholded), although such a large difference was not noticed for the other samples in the study (Figure 7). To investigate this, further data consisting of a pair of montages collected from the same area, but with different contrast and brightness, were obtained. One with normal contrast and the second with a higher contrast was designed to expand details at the darker end of the grey-level scale. For the standard contrast BSE montage, thresholding for organics (dark areas) resulted in too high a level (78%), while the montage with higher contrast returned a lower value of 45% (Figure 9), with the latter being in close agreement with that of the recorded TOC (Figure 7). This illustrates the sensitivity of some organic laminated mudstones to contrast/brightness settings and position of threshold applied.

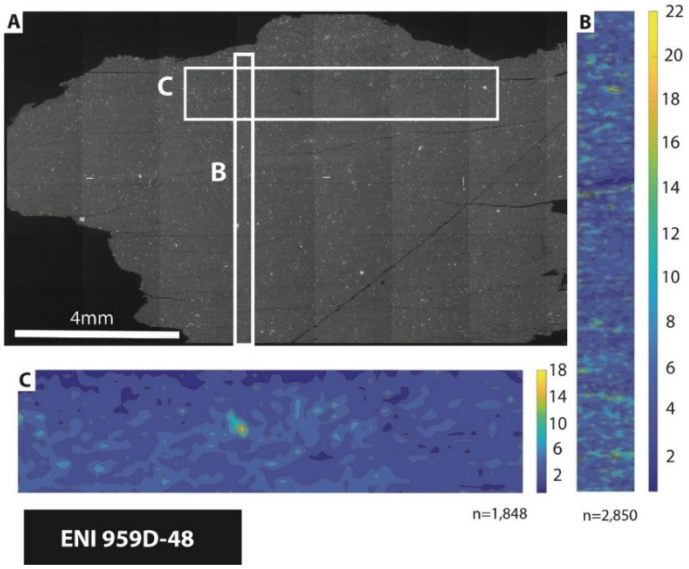

Figure 8. (**A**) Backscattered montage of large area of sample 959D-48. (**B**,**C**) are colour contoured maps for organics, from tile sets collected from areas B and C in (**A**), with 1848 and 2850 tiles, respectively. Individual tile horizontal field of view (HFOV) 60 µm.

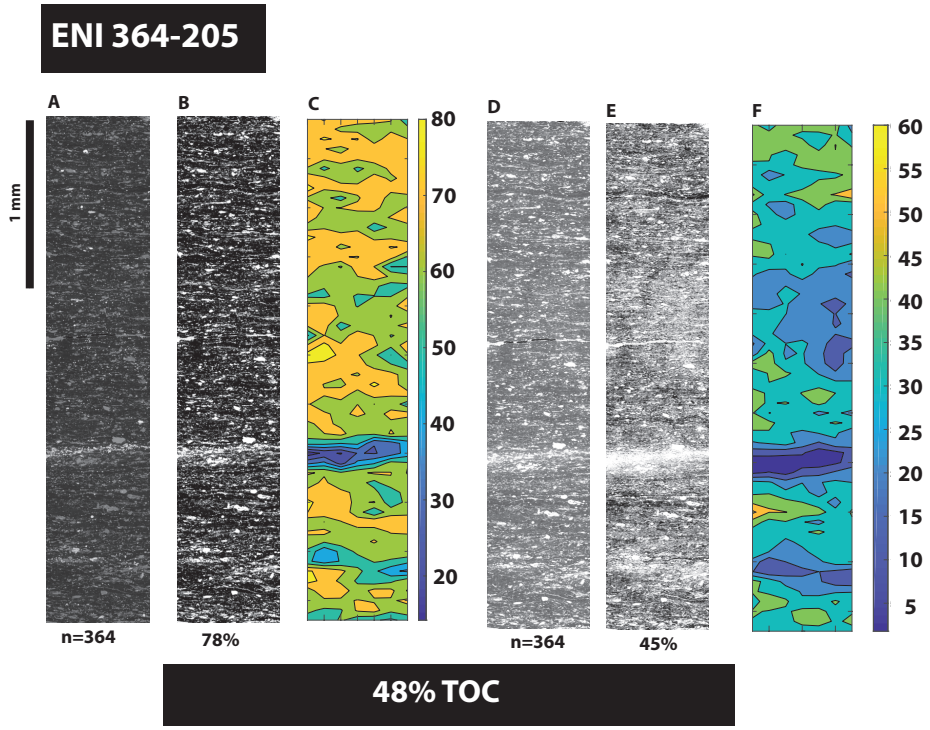

Figure 9. (**A**,**D**) representative area, BSE montages (364 tiles, each with 100 µm HFOV) of the same area, across thin-section of sample #364-205, with normal contrast (**A**), and expanded contrast to expand detail at the darker end of the spectrum (**D**). (**B**,**E**) binarized (for organics) of (**A**,**D**). (**E**) with mid-range threshold, binarized and despeckled. (**B**,**E**) with 78% and 45% organics, respectively. (**C**,**F**) colour contoured map, constructed based on individual tiles from (**B**,**E**).

In low TOC mudstones, organic material occurs as isolated particles, which potentially could be problematic when trying to differentiate from pores or empty foraminifera chambers (with or without epoxy resin fill), or plucked silt grains. For both low and higher TOC samples, there is a potential problem where thicker resin filled cracks are present, and to a lower extent, fine bedding parallel cracks may add to the calculated value for organic content. In the case of all samples examined herein, cracks were mitigated through thresholding by not selecting the darker pixels, but by selecting more intermediate dark grey pixels. This results in most larger and smaller cracks not being selected, although it will not necessarily be possible to exclude all cracks, resulting in a proportion of false positives for organic material. In addition, although selecting the majority of organic particulates, this method of thresholding results in underrepresentation of the organic particulates. This can be partially alleviated through use of the noise despeckle function in 'Fiji', although typically the degree of organic particulates is still underrepresented. Nevertheless, the two tend to cancel each other out, and the average organic percentage agrees well with that recorded by TOC.

New methodologies may need to be developed to take into consideration shape and size parameters through further image analysis, and to differentiate true organic material from cracks and other features. Alternative procedures, such as the use of low kV BSE imaging, or possibly even secondary electron (SE) imaging, may help to enhance contrast between organic material and thin-section impregnation resins. However, as illustrated, this method has good potential in the area of organic particle analysis for both low and high TOC mudstones.

3.3. User Bias

Both of the examples illustrated (pyrite and organic material) depend upon user influenced thresholding for selecting either pyrite or organic material. In both cases, this will introduce a small amount of user bias, with the degree of bias hard to accurately define. It may be possible for specific issues to fabricate standards for calibration purposes, and to use these to better constrain thresholding parameters. In addition, to try and negate user bias, it is possible to use mean grey-level (MGL), which is calculated for each tile and plotted as a coloured contoured map (Figure 10). In these cases, areas with higher pyrite occurrence will have higher mean grey-level values. For organic 'rich' material, those with higher organic content will have a lower value (not illustrated). Although the use of mean grey-value will minimise user bias, no percentage occurrence values are obtained using this method.

Mean grey-level may also reflect relative changes in the dominance of detrital silicates (silt), clays, carbonates (biological calcite, authigenic dolomite), porosity (Figure 11) or localized unloading or weathering cracks, as well as pyrite, organic material. The identification of the particular cause of mean grey-level variation may not be directly evident. Further examination of BSE images, and possible EDX analysis, could be required to determine likely controls over changes in the distribution of the mean grey-level, which can be confirmed through the thresholding of BSE images, and the plotting of further colour contoured maps for the variation in percentage occurrence of likely candidate phases. Nevertheless, the use of mean grey-level in many cases would offer a quick look at potential variability within a polished thin-section, which does not require additional processing (thresholding) and, therefore, is not susceptible to the addition of operator bias and may be useful for corroborating thresholded data.

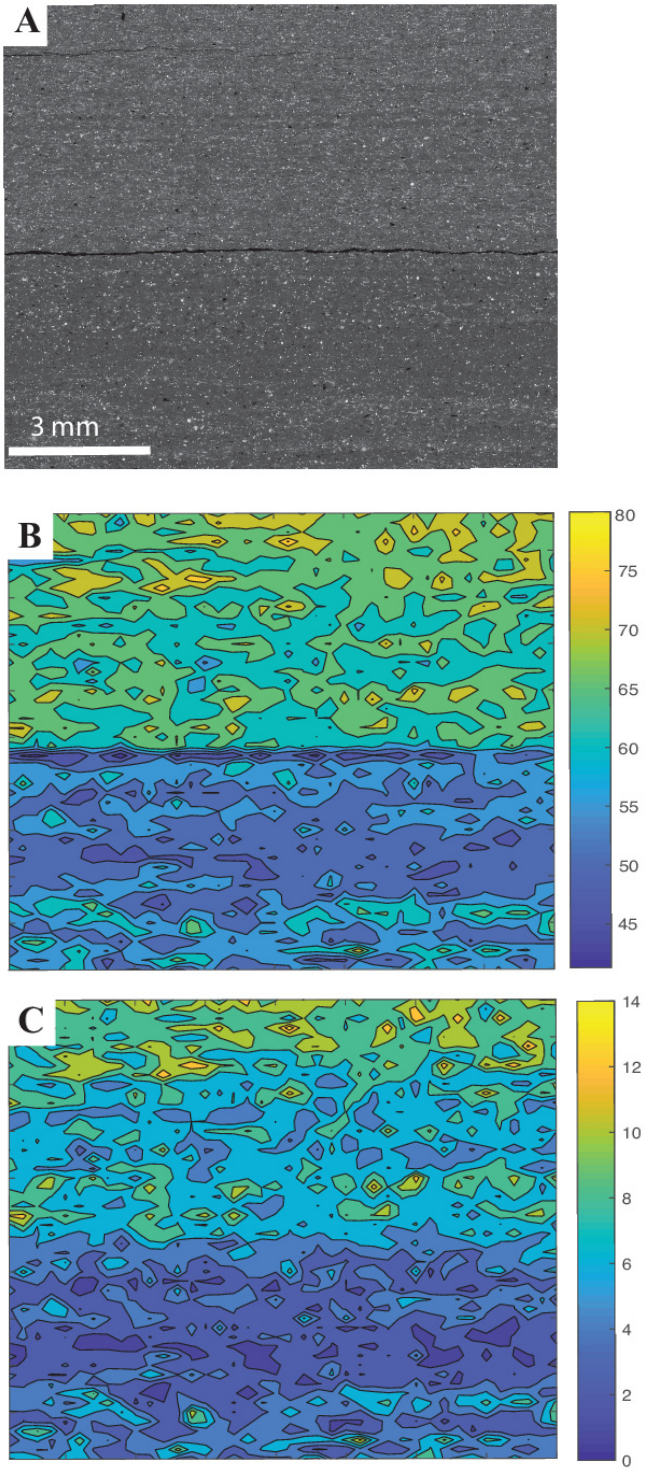

Figure 10. Jurassic mudstone sample #9 with (**A**) BSE montage, (**B**) mean grey-level (0–256) colour contour map and (**C**) pyrite percentage colour contour map. Each montage comprises 6557 tiles, with 200 μm HFOV.

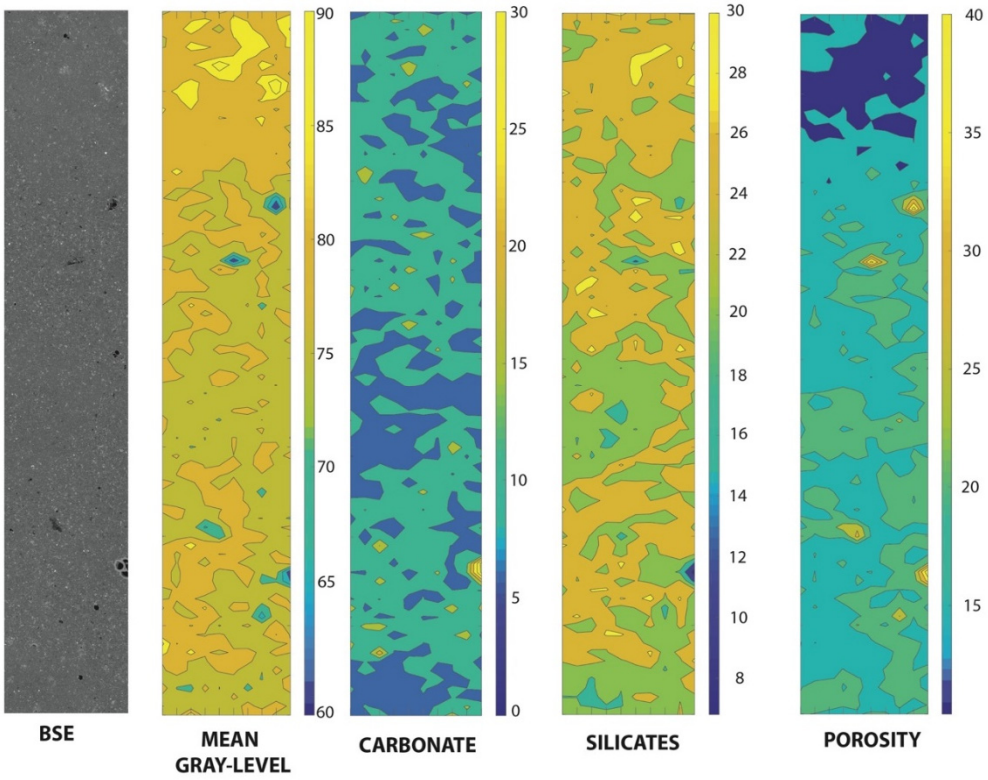

Figure 11. Montage through muddy contourite, from the Bay of Cadiz. From left to right: BSE montage, mean grey-level colour contour map, carbonate%, silicates% and porosity% colour contour maps. Montage and colour contoured maps comprise 800 tiles, each with a 300 μm HFOV.

3.4. Significance of Tile Size

The size of individual tiles directly controls the type and level of detail that can be extracted from the constructed coloured contoured maps. Variations in the distribution of pyrite typically require the acquisition of tiles with a horizontal field of view of 200–300 microns (1536 pixels). Whereas, a field of view of 1–2 mm (768 pixels) can be sufficient when looking for larger scale changes in mineralogy (percentage calcite, silicates) or porosity. In the case of organic material, a horizontal field of view of 100 microns (1536 pixels) was found to be sufficient, although this tile size is too large to pick out individual micron scale organic lamination. The latter would require the use of tiles with a horizontal field of view in the order of 1–2 microns (768 pixels), which would be impractical and too time consuming over larger areas.

3.5. Atomic Number

Pyrite and organics are reasonably simple to threshold. However, consideration of the mean atomic number (Z) for a range of common mineral phases occurring within sedimentary rock systems (Figure 12) illustrates the potential for the separation of phases by thresholding based on the grey-level within BSE images. According to Krinsley et al. [25], modern BSE detectors can typically resolve differences in Z = 0.1. Therefore, it is clear that the heavier phases, such as rutile, goethite, hematite and pyrite, should as a group be easily separated from clays, clastic particles and carbonates within mudstones. Distribution of pyrite (FeS_2) is easily illustrated through the thresholding of the brightest particles in the acquired BSE images. Where other high atomic number phases (heavy minerals such as zircon and ilmenite, or other phases such as iron-oxides, iron/lead/zinc-sulphides) are present in appreciable numbers, then maps for pyrite may not be an accurate reflection of the true distribution. In such cases, separation of brighter (heavier atomic number) phases may be differentiated by more careful contrast-brightness setting selection of BSE tiles prior to image scanning in order to maximise

differences between the brighter phases and minimise atomically lighter (darker grey) phases, although some difficulty may exist with the separation of hematite and pyrite. Similarly, most of the 'clays' (montmorillonite, kaolinite and Mg chlorite) can simply be separated from other phases of interest, while illite and Fe chlorite with higher Z values can also be differentiated from other close phases (see Figure 12). Problems may, however, exist in the clean separation of albite and quartz, as well as of quartz from dolomite, as these vary at less than 0.1 Z difference. Therefore, from a practical point of view, albite lamellae/regions within orthoclase feldspars would likely be thresholded as quartz, as would albite feldspar grains, and quartz and dolomite may not be separated. Problems will also be further compounded if thin-sections are poorly polished, or where bevelled grain margins are produced between phases of differing hardness, as both will broaden the observed grey-level for any given phase due to variation in surface orientation [25]. Further consideration of the data in Figure 12 also illustrates that it will not be possible to simply threshold for clastic silicates (quartz, feldspar, mica) or carbonates (calcite, dolomite, siderite) due to the wide range of Z-values across the two groups. In the case of both calcite and dolomite, thresholding can be further compromised by zonation with dolomites, and in the biologically produced calcite variation in Z-value caused by the presence/absence of Mg, organics or micro-porosity.

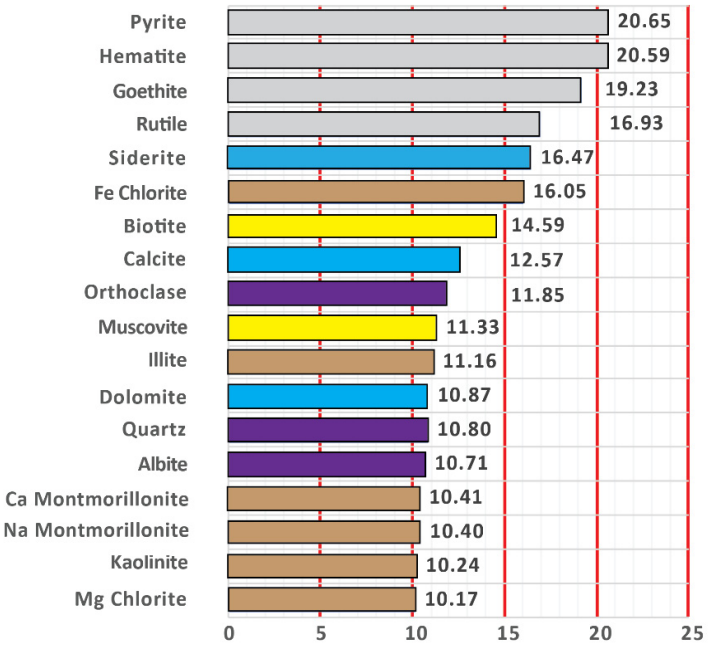

Figure 12. Mean atomic number (Z) for a range of common mineral phases occurring within sedimentary rock systems, after data from Krinsley et al. [25].

4. Conclusions

High-resolution BSE images (tiles), collected during automated acquisition from large areas (10's mm^2), can be reprocessed to extract additional information on the distribution of mineral phases within polished thin-sections of mudrocks. Simple image analysis, with thresholding for phases such as pyrite and organic materials, is easily applied to determine the percentage of coverage for the phase of interest, which can then be plotted with the aid of software such as 'MATLAB' to produce colour contoured maps that visually illustrate the changes in distribution of such phases with respect to position on the slide/scanned area. Results can be compromised by poor sample preparation, the presence of cracks and can require careful consideration of thresholding issues and the potential for user bias. Nevertheless, the technique allows any heterogeneities (vertical and lateral) to be easily quantified in a far more accessible format than simply constructing large area high-resolution BSE montages.

Data on percentage coverage from each tile can also be used as an alternative to the collection of phase concentration from bulk samples, such as TOC and total percentage pyrite.

This technique has wider application to mudrock than just pyrite and organic distribution, and can also be used to examine heterogeneity and distribution of porosity and carbonate, as well as silicate grain distributions, across a wide range of environments such as lacustrine, shallow marine and deep-water settings. It also has application to carbonate rocks [20], and is likely to have potential in other rock groups such as igneous and metamorphic rocks, as well as other porous media.

Author Contributions: Conceptualization, J.B.; methodology, J.B., A.A., O.E.; software, J.B.; validation, J.B.; formal analysis, J.B.; investigation, J.B.; resources, J.B., T.W., A.A., O.E.; writing—original draft preparation, J.B.; writing—review and editing, J.B., A.A., O.E., T.W.; supervision, J.B., T.W.; funding acquisition, G.G. All authors have read and agreed to the published version of the manuscript.

Funding: We thank IFP Energies Nouvelles and Eni SpA for financial support of this study.

Acknowledgments: The Centre for Environmental Scanning Electron Microscopy (CESEM) is thanked for access and use of scanning electron microscopy and computer facilities. We acknowledge Violaine Lamoureux-Var from IFP Energies Nouvelles for continuous, constructive discussions throughout this project. The International Oceanic Drilling Program (IODP) is acknowledged for access to materials.

Conflicts of Interest: The authors declare no conflict of interest. We thank IFP Energies Nouvelles and Eni SpA for permission to publish the current work.

References

1. Pettijohn, F.J. *Sedimentary Rocks*; Harper: New York, NY, USA, 1967.
2. Blatt, H. *Sedimentary Petrology*; W.H. Freeman and Company: San Francisco, CA, USA, 1982.
3. Franklin, J.A. *Evaluation of Shales for Construction Projects: An Ontario Shale Rating System*; Report RR229; Research and Development Branch, Ministry of Transportation and Research: Toronto, ON, Canada, 1983; p. 9.
4. Ibbeken, H.; Schleyer, R. *Source and Sediment: A Case Study of Provenance and Mass Balance at an Active Plate Margin (Calabria, Southern Italy)*; Springer: New York, NY, USA, 1991; p. 286.
5. Komameni, S.; Roy, D.M. Shale as a radioactive waste repository: The importance of vermiculite. *J. Inorg. Nucl. Chem.* **1979**, *41*, 1793–1796. [CrossRef]
6. Al-Rawas, A.; Cheema, T.; Al-Aghbari, M. Geological and Engineering Classification Systems of Mudrocks. *Sci. Technol. Spec. Rev.* **2000**, *5*, 137–155. [CrossRef]
7. Al-Bazali, T.M.; Zhang, J.; Chenevert, M.E.; Sharma, M.M. Measurement of the sealing capacity of shale caprocks. In Proceedings of the SPE Annual Technical Conference and Exhibition, Dallas, TX, USA, 9–12 October 2005.
8. Delage, P.; Cui, Y.J.; Tang, A.M. Clays in radioactive waste disposal. *J. Rock Mech. Geotech. Eng.* **2010**, *2*, 111–123. [CrossRef]
9. Olabode, A.; Bentley, L.; Radonjic, M. Shale caprock integrity under carbon sequestration conditions. Porous Media and its Applications in Science, Engineering, and Industry. *Am. Inst. Phys. Conf. Proc.* **2012**, *1453*, 347–352.
10. Wagner, T.; Floegel, S.; Hofmann, P. Marine black shale and Hadley Cell dynamics: A conceptual framework for the Cretaceous Atlantic Ocean. *Mar. Pet. Geol.* **2013**, *43*, 222–238. [CrossRef]
11. Zou, C.; Yang, Z.; Dai, J.; Dong, D.; Zhang, B.; Wang, Y.; Deng, S.; Huang, J.; Liu, K.; Yang, C.; et al. The characteristics and significance of conventional and unconventional Sinian-Silurian gas systems in the Sichuan Basin, central China. *Mar. Pet. Geol.* **2015**, *64*, 386–402. [CrossRef]
12. Camp, W.K.; Diaz, E.; Wawak, B. *Electron Microscopy of Shale Hydrocarbon Reservoirs, Memoir 102*; The American Association of Petroleum Geologists: Tulsa, OK, USA, 2013; p. 260.
13. Milliken, K. A compositional classification for grain assemblages in fine-grained sediments and sedimentary rocks. *J. Sediment. Res.* **2014**, *84*, 1185–1199. [CrossRef]
14. Lazar, R.; Bohacs, K.M.; Schieber, J.; Macquaker, J.; Demko, T. Mudstone primer: Lithofacies variations, diagnostic criteria, and sedimentologic-stratigraphic implications at lamina to bedset scale. *SEPM Concepts Sedimentol. Paleontol.* **2015**, *12*, 200.
15. Milliken, K.L.; Ergene, S.M.; Ozkan, A. Quartz types, authigenic and detrital, in the Upper Cretaceous Eagle Ford Formation, South Texas, USA. *Sediment. Geol.* **2016**, *339*, 273–288. [CrossRef]

16. Ma, L.; Fauchille, A.L.; Dowey, P.; Figueroa Pilz, F.; Courtois, L.; Taylor, K.G.; Lee, P.D. Correlative multi-scale imaging of shales: A review and future perspectives. *Geol. Soc. Lond. Spec. Publ.* **2017**, *454*, 175–199. [CrossRef]
17. Lemmens, H.; Richards, D. Multiscale imaging of shale samples in the scanning electron microscope. In *AAPG Memoir, 102; Electron Microscopy of Shale Hydrocarbon Reservoirs*; Camp, W., Diaz, E., Wawack, B., Eds.; The American Association of Petroleum Geologists: Tuksa, OK, USA, 2013; pp. 27–35.
18. Buckman, J.; Mahoney, C.; Bankole, S.; Couples, G.; Lewis, H.; Wagner, T.; März, C.; Blanco, V.; Stow, D. Workflow model for the digitization of mudrocks. *Geol. Soc. Spec. Publ.* **2018**, *484*. [CrossRef]
19. Buckman, J.; Busch, A. Improved visualization of heterogeneity within shales: Colour contoured maps constructed from large area high-resolution SEM montages. In Proceedings of the Sixth EAGE Shale Workshop, Bordeaux, France, 28 April–1 May 2019.
20. Buckman, J.; Bankole, S.A.; Zihms, S.; Lewis, H.; Couples, G.; Corbett, P.W.M. Quantifying porosity through automated image collection and batch image processing: Case study of three carbonates and an aragonite cemented sandstone. *Geosciences* **2017**, *7*, 70. [CrossRef]
21. Buckman, J.; Charalampidou, E.-M.C.; Zihms, S.; Lewis, M.H.; Corbett, P.W.M.; Couples, G.D.; Jiang, Z.; Huang, T. High-resolution large area scanning electron microscopy: An imaging tool for porosity and diagenesis of carbonate rock systems. In *Carbonate Pore Systems: New Developments and Case Studies*; SEPM Society for Sedimentary Geology, SEPM Special Publications: Tulsa, OK, USA, 2017.
22. Aboussou, A.; Lamoureux-Var, V.; Wagner, T.; Pillot, D.; Kowalewski, I.; Marz, C.; Garcia, B.; Doligez, B. Application of an advanced method for pyrite and organic Sulphur quantification to organic rich marine sediments (extended abstract). In Proceedings of the 80th EAGE Conference & Exhibition 2018, Copenhagen, Denmark, 11–14 June 2018.
23. Vandenbroucke, M.; Largeau, C. Kerogen origin, evolution and structure. *Org. Geochem.* **2007**, *38*, 719–833. [CrossRef]
24. Krom, M.D.; Berner, R.A. A rapid method for the determination of organic and carbonate carbon in geological samples. *J. Sediment. Petrol.* **1983**, *53*, 660–663. [CrossRef]
25. Krinsley, D.H.; Pye, K.; Boggs, S.; Tovey, N.K. *Backscattered Scanning Electron Microscopy and Image Analysis of Sediments and Sedimentary Rocks*; Cambridge University Press: Cambridge, UK, 1998; p. 193.